# Experimental study of isothermal vertical slug flow

Iztok Tiselj, Jan Kren, Blaž Mikuž
*Jožef Stefan Institute*
*Jamova 39, 1000 Ljubljana, Slovenia*
*iztok.tiselj@ijs.si; jan.kren@ijs.si; blaz.mikuz@ijs.si*

**Abstract** – *Large gas bubbles separated by the liquid slugs are the main characteristic of the slug flow regime. We have analyzed the stagnant Taylor bubble in the vertical isothermal turbulent counter-current flow with high speed videos at 100 to 800 frames per second. A single Taylor bubble was captured in each experiment through dynamical balance of the bubble drag in the downward liquid flow. Bubbles of around two to six diameters length were observed in the pipe of 26 mm diameter with liquid Reynolds numbers in front of the bubble around 6000. Video frequencies at around 400 Hz were found sufficient to capture all temporal fluctuations of the bubble interface. Algorithms for two-phase interface recognition have been developed and applied on the images of the cap and the body of the Taylor bubbles. We have observed asymmetric Taylor bubbles of bullet-train shape with the thinnest liquid film on the belly of the bullet-train shape bubble. Even the long time averaging of up to 10 minutes did not produced axisymmetric time-averaged shape of the bubble in turbulent liquid flow. Azimuthal position of the bubble's belly is randomly determined during the injection of the bubble into the test section. In addition, dynamics of the tiny disturbance waves with tenth of mm amplitudes has been tracked along the interface of the Taylor bubbles. Cross-correlations of time-dependent interface fluctuations were measured at different spatial positions and used to determine propagation speeds of the traveling interface waves.*

**Keywords:** counter-current slug flow, Taylor bubble, shadowgraphy

## I. Introduction

Gas-liquid mixture flows exhibit various two-phase flow patterns, with vertical pipes commonly experiencing bubbly, slug, churn, annular, and droplet flow regimes [1]. The specific flow regime depends on factors such as flow velocities, phase volume fractions, fluid properties, and pipe size and orientation. This study focuses on Taylor bubble flow, which falls under the slug flow regime. Taylor bubbles are bullet-shaped bubbles that move at different speeds than the bulk liquid, occupying almost the entire pipe cross-section. Slug flows are encountered in a wide range of practical applications, including vaporizers, boilers, filtration and membrane processes [2], as well as extreme events in the petroleum industry [3] or steam generators in nuclear power plants.

All experiments mentioned in the present paper are conducted in the inertia dominant regime, where the influence of viscosity and surface tension is minimal [1]. In this regime, the drift velocity of Taylor bubbles $U_0$ in pipe with diameter $D$, is given by the correlation $U_0 = k\sqrt{gD}$ ($g$ acceleration of gravity). Based on the constant value of $k$=0.35, this correlation predicts a drift velocity of approximately 0.18 m/s for Taylor bubbles in our experiments [4]. This value is close to the average measured liquid velocity, $U_L$, which is in the downward direction (negative sign) and keeps the bubble fixed in position. This type of flow is known for the unstable and asymmetric Taylor bubble behavior [5].

One of the earliest experiments on counter-current turbulent flow was conducted by Martin in 1976 [6]. The study investigated air-water mixtures in circular pipes with diameters of D = 2.6, 10.16, and 14.0 cm.

Martin demonstrated that the velocity of the bubble in the counter-current slug flow could not be adequately represented by co-current background flow or stagnant liquid theories. This is attributed to the instability of the bubble, which increases its velocity when pushed away from the pipe axis. Analytical stability analysis in [7] showed that the symmetry of the Taylor bubble breaks down at liquid velocities lower than the critical negative velocity of $U_c = -0.13\sqrt{gD}$.

The interactions between Taylor bubbles and turbulent liquid flow have been the subject of various studies. Unlike in laminar liquid flow, the skirt of the bubble starts to break up in the turbulent background flow. The breakup and recoalescence processes in the bubble wake region have been observed. The studies [8,9] measured the gas loss from a stationary Taylor bubble in a counter-current liquid flow using a special spherical Teflon cap to hold the bubble in a fixed position. More recent experiments involving the turbulent counter-current regime have utilized high-speed cameras in visible light to measure the bubble's disintegration rate [10]. By dynamically controlling the liquid flow rate, the bubble can remain trapped in an equilibrium position for hours, allowing for studies over several minutes.

## II. Experimental Setup

The experiment was conducted in a loop, as depicted in Figure 1. The test section consisted of a 1.5 m long glass pipe with an internal diameter of D=26 mm. To maintain a constant water temperature of 30°C, a heat exchanger was utilized in the tank. The mass flow rate was measured at a frequency of 1 Hz using a Coriolis flow meter. All experiments were performed in the turbulent flow regime of the liquid above the bubble, with a Reynolds number of approximately 6000. The straight section of the pipe above the bubble spanned around 40 pipe diameters, ensuring statistically uniform turbulence impinging on the bubble. The Taylor bubble was injected into the test section from a dead end pipe installed beneath it. The flow through the test section was manually regulated using a control valve, which adjusted the flow distribution between the main loop and a bypass loop.

Observations of the Taylor bubble were carried out using a high-speed camera with a field of view covering a 14 cm (~5D) section of the pipe. To minimize optical distortion, the pipe was immersed into a rectangular glass section filled with water. The

camera's useful resolution for the measurements was approximately 1280x240 pixels, corresponding to around 9 pixels/mm. The observed Taylor bubbles typically had lengths ranging from 1.5D to 4D. Measurements were performed over different time intervals of 8, 4, 2, and 1 minute, with camera frequencies of 100, 200, 400, and 800 Hz, respectively.

The measurement of absolute liquid film thickness is achieved with a precision ranging between 0.5 and 1 pixel. However, this level of precision introduces relative errors exceeding 40% for very thin films below 3 pixels. The estimated optical distortion, due to the light refraction, results in a maximum enlargement of the liquid film thickness by up to 2%. This value is significantly lower than the uncertainty associated with interface reconstruction.
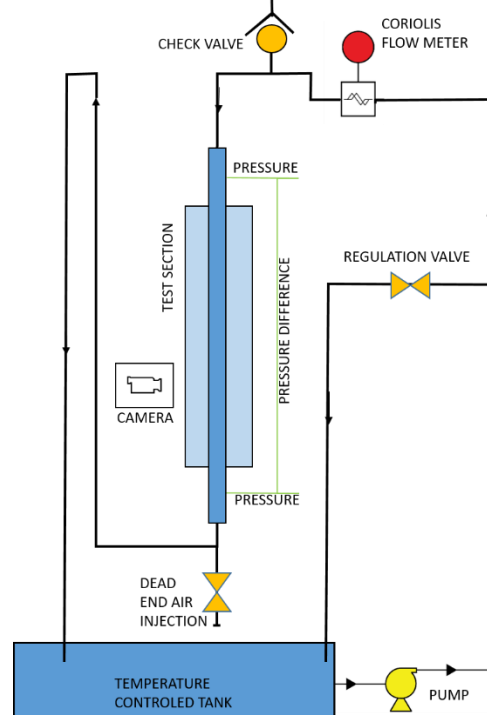


*Fig. 1. Schematics of the test loop.*

In the counter-current flow configuration, the instability of the Taylor bubble requires dynamic adjustments of the mass flow rates during the experiment to ensure the bubble remains within the camera's field of view. Minor corrections to the valve positions are made every few seconds, leading to fluctuations in the bulk liquid velocity within the test section. The bulk liquid velocity is measured based on the readings from the Coriolis flow meter. The statistical dispersion (Root-Mean-Square) of the mean velocity measurement is fluctuating between 3% and

10% of the bulk velocity between various experimental cases. While this technique of bubble position control may present challenges when comparing results with similar experiments or numerical simulations, it closely resembles the numerical technique employed in high-fidelity simulations of co-current Taylor bubble flow [13]. In these simulations, the Taylor bubble is modeled within a moving frame of reference to ensure the bubble remains inside the computational domain.

## II.A. Image Processing

The processing of each recording involved analyzing a set of 50,000 photographs using our dedicated in-house software. This software utilized widely used libraries for tasks such as fitting two-dimensional surfaces and one-dimensional lines, performing Fourier transformations, and cross-correlating one-dimensional functions. The algorithms and techniques employed in the software were based on methods described in the Numerical Recipes book [14].

The main focus of the computer codes was image processing, specifically the extraction of the Taylor bubble surface from the images. Given the constraints of automated analysis on a large dataset, we made use of established image processing methods found in open literature [15]. In order to handle the large number of photographs, manual corrections and artifact removal were limited. To address this, we developed a robust procedure that could identify potential failures in bubble interface reconstruction. Description of the algorithm can be found in [17], while the intermediate results of the particular step of silhouette reconstruction are shown in Fig. 2:

- a=>b: conversion of image density matrix into gradient matrix .
- b=>c: identification of the bubble outer surface
- c=>d,e: sub-pixel interface position refinement.

Distinguishing between absolute and relative accuracy is crucial when considering interface recognition. The absolute uncertainty of the interface position on a single photography ranges from half a pixel to one pixel. However, when analyzing a time series or spatial profiles of the interface, the relative uncertainty of the interface motion between neighboring pixels in space or time is reduced by a factor of approximately 5 or $\pm 0.1$ pixel. This improvement in relative accuracy allows very precise characterization of interface movements.
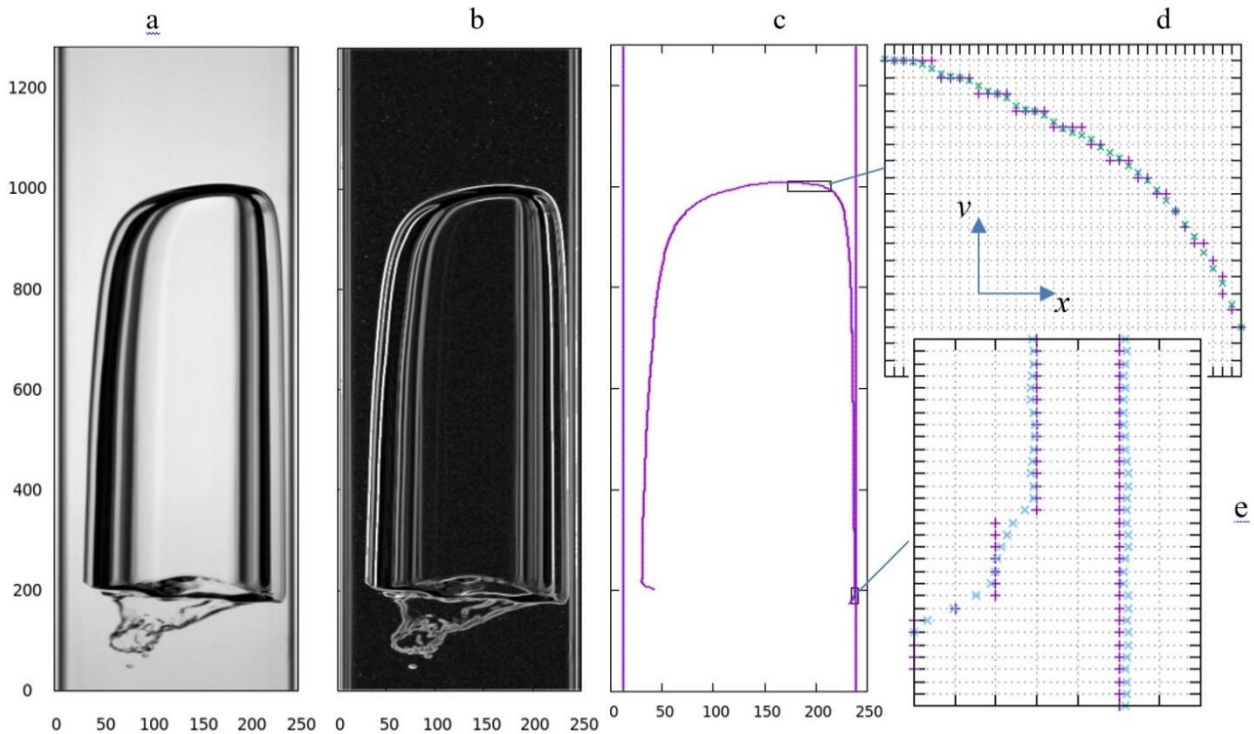


Fig. 2: a) original image, b) magnitude of the gradients field (step 1), c) extracted bubble interface and pipe inner walls at pixel level (step 2), d, e) refinement of the interface position at subpixel level (step 3) with pixel grid in the background: violet "+" - pixel level interface, blue and green "x" - sub-pixel level interface. All units in pixels.

# III. Results

## III.A. Time Averaged Taylor Bubble Shape

Due to inherent instabilities, maintaining the Taylor bubble at a fixed vertical position with a constant mass flow rate was not feasible during our measurements. Instead, we employed manual adjustments of the mass flow rate to keep the bubble within the observation region. The characteristic movements of typical Taylor bubbles in our experiments are depicted in the graphs of Figure 3. These bubbles exhibit vertical velocities of approximately 0.01 m/s, which are considerably lower than the upstream mean liquid velocity of 0.18 m/s and the velocities around 1 m/s observed on the liquid-air interface of the Taylor bubble.
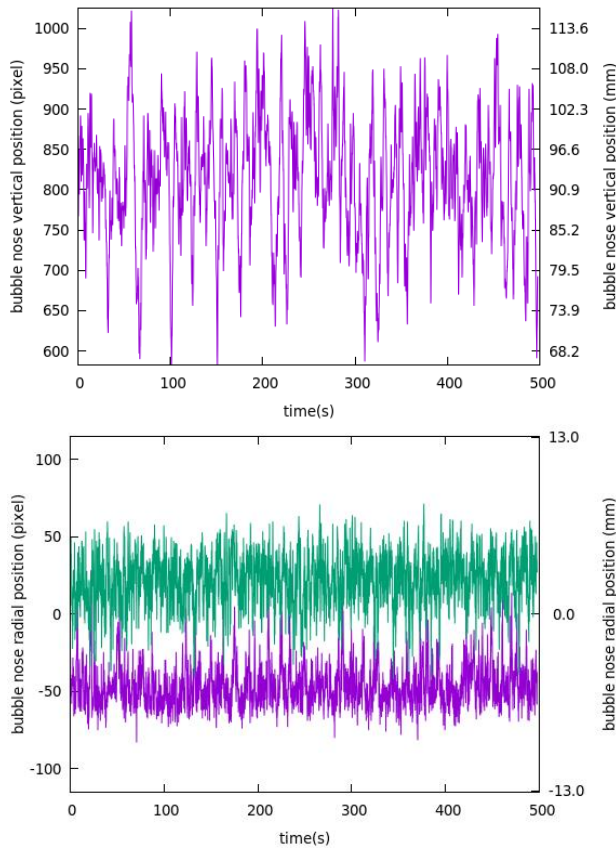


*Fig. 3: Top: typical bubble nose vertical position measured from the bottom line of the camera field of view. Bottom: distance of the bubble nose from the pipe axis for typical measurements (2D-10(1) and 2D-10(2) in Table 1)*

The bottom image of Figure 3 illustrates the radial position of the bubble nose during two 8-minute measurements. In an axisymmetric scenario, the nose of the bubble would remain fixed at r=0. However, as observed in Figure 3, the bubble noses exhibit a quasi-stable asymmetric position. In the specific case depicted, one bubble is inclined towards one side of the two-dimensional projection while the other bubble is inclined towards the opposite side. Occasionally, the noses of both bubbles cross the axis; however, on average, they remain attached to their respective sides of the pipe throughout the 8-minute time interval. This persistent asymmetry was consistently observed, indicating that once a bubble became attached to a particular side of the pipe, it tended to remain there for an extended period, despite occasional radial movements. Similar findings were observed for other bubbles considered in our study, where the asymmetric position and azimuthal orientation attained during the bubble injection phase remained unchanged throughout the measurement.

*Table I Experimental runs by name, camera frequency and Taylor bubble length.*

| measurement case | camera freq. (Hz) | Bubble length (D) |
|---|---|---|
| 8*2D-10 (8 cases) | 100 (effective 10) | 2D |
| 2D-200 | 200 | 2D |
| 2D-400 | 400 | 2D |
| 4D-200 | 200 | 4D |
| 4D-400 | 400 | 4D |
| 4D-800 | 800 | 4D |

The initial objective of our research was to predict the time-averaged shape of the Taylor bubble in turbulent counter-current flow, aiming for an axisymmetric configuration. This information could have been valuable for validating computational fluid dynamics (CFD) models developed to investigate the same phenomena. However, as illustrated in the bottom image of Figure 3, we were unable to obtain axisymmetric time-averaged images of the Taylor bubble within 8-minute intervals.

To mitigate the asymmetry, we attempted a combination of time averaging and ensemble averaging to derive a less skewed shape for the time-averaged bubble. For ensemble averaging, we conducted a series of eight measurements referred to as "2D-10 cases" in Table 1. These measurements were captured at a camera frequency of 10 Hz, storing 1 out of every 10 images, and spanning over 8-minute intervals. Time averaging was performed for each case, and the resulting data sets were merged through ensemble averaging to form a single set of data depicted in Figure 4, denoted as "8*2D-10" in Table 1.

These measurements encompassed four distinct bubbles. The ensemble-averaged bubble shape shown in Figure 4 exhibits improved axial symmetry compared to most individual bubbles. However, even in this case, the ensemble average is tilted towards the right wall. Consequently, we conclude that achieving an axisymmetric time-averaged shape for the Taylor bubble is not feasible under the conditions of our
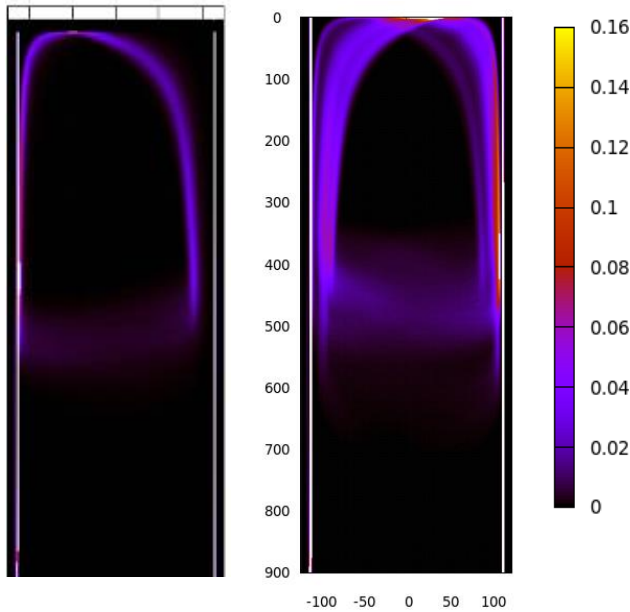


experiments.

*Fig. 4: 8\*2D-10 case. Left: Taylor bubble interface position obtained with time averaging of one measurement case. Right. Ensemble average of eight time averaged fields. Color scale: share of photos with interface location at given pixel position (max = 1). Length units in pixels.*

It is worth noting that additional ensemble averaging may potentially lead to enhanced axial symmetry. Nevertheless, applicability of such an approach is questionable, as any numerical simulation or similar experiment would ultimately yield asymmetric time-averaged results if time averaging is employed without ensemble averaging.

The asymmetry observed in the time-averaged Taylor bubble, as depicted in Figure 4, presents challenges when it comes to independently verifying our measurements. However, we have found a way to mitigate this issue by averaging both sides of the silhouettes, resulting in results that are less affected by the asymmetry. These findings are presented in Figure 5, which illustrates the liquid film thickness along the bubble. To achieve this, we combined time averaging, ensemble averaging, and left-right side averaging of

our photographs. The axial distances along the x-axis of Figure 5 are measured from the bubble nose. The thick violet profile represents the time-averaged, ensemble-averaged, and left-right averaged profile derived from the measurements in Figure 4.
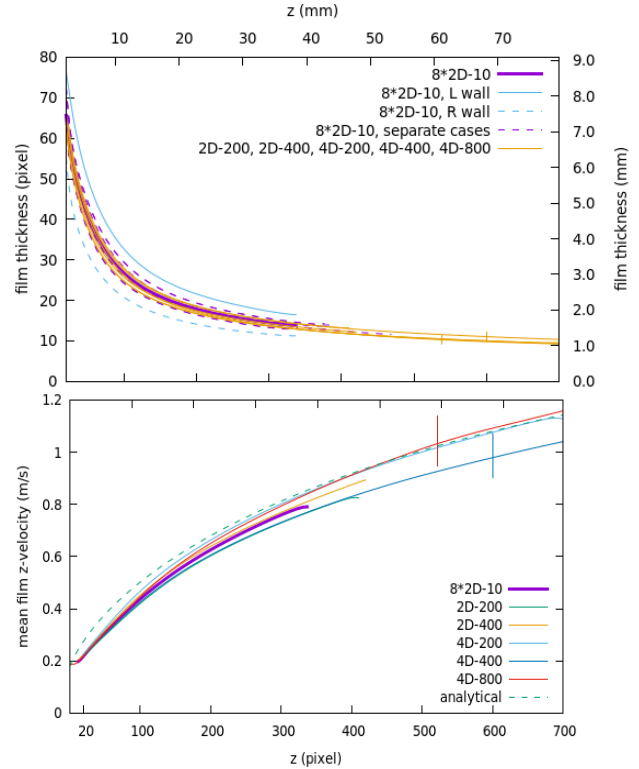


*Fig. 5: Top: Average liquid film thickness of 13 bubbles from Table 1. Measurement uncertainty is not plotted, but is below 1 pixel (0.1 mm). Bottom: Mean downward liquid film velocity (m/s) based on film thickness measurements and continuity equation.*

Additionally, two blue lines, which depict the envelopes of all other curves, represent the time-averaged and ensemble-averaged profiles for the left and right sides separately from the 8\*2D-10 case. It is noteworthy that all eight dashed violet curves, which represent the left-right averaged profiles for each measurement of 8\*2D-10, as well as the five orange curves from Table 1 included in Figure 5, fit within the envelopes. This analysis demonstrates that the left-right averaged curves align well with the overall trends captured by the time and ensemble averaging process. By incorporating this approach, we have successfully reduced the impact of the asymmetry on our results, thus improving the reliability of our measurements.

By utilizing the measured and averaged film thickness profiles, we can derive an additional curve related to the mean downward liquid velocity in the

film region. Based on the continuity equation and known upstream liquid velocity, the mean liquid velocity can be calculated as $v(z) = v_0 R^2 / [2Rh(z) - h(z)^2]$, where $R$ represents the pipe radius ($R$ = 13 the bubble ($v_0$ = 0.18 m/s), and $h(z)$ represents the liquid film thickness at a given axial position $z$. By assuming the measured film thickness, we can calculate the mean liquid velocity within the film region. The bottomgraph of Figure 5 presents the mean liquid velocity profiles separately for the time-averaged, ensemble-averaged, and left-right averaged film derived from the measurements listed in Table 1. The time-averaged liquid film thickness serves as a reasonably accurate measure of the bubble diameter, making it applicable for evaluating the mean velocity within the liquid film. Consequently, the relative uncertainty of the time-averaged mean film velocity profiles is similar in magnitude to the uncertainty of the mean film thickness measurements, approximately 10% at distances greater one diameter D from the bubble nose.

The dashed curve in the bottom image of Figure 5, labeled as "analytical," represents an approximate solution derived from the simplified film momentum equation [17]. This equation considers the film near the Taylor bubble as a free-falling film influenced by gravity and opposed by wall shear stress, neglecting the shear of the air within the bubble. The agreement observed between the measurements and the profile obtained from the analytical model indicates that the neglected air-liquid shear at the bubble interface is likely minimal.

The time-averaged bubble shapes discussed in this section deviated from our initial expectations of axial symmetry becoming more apparent with sufficiently long time averaging. This deviation was not due to experimental uncertainties but rather stemmed from the physics of the Taylor bubble in counter-current turbulent flow. The quasi-stable asymmetries observed in the positions of the bubble over several-minute intervals resulted in asymmetric time-averaged bubble shapes. Consequently, our two-dimensional approach yielded useful results by averaging the bubble shape and corresponding liquid film thickness over both sides of the photographs. This approach provided relatively accurate liquid film thickness measurements with reasonably small statistical dispersion across various Taylor bubbles.

To achieve ideal averaging of the three-dimensional bubble shape, stereoscopic measurements and recognition of the full three-dimensional bubble shape would be required. Such an approach would eventually lead to an asymmetric bubble shape that could be directly compared to future measurements or three-dimensional simulations.

### III.B. Disturbance waves on bubble surface

Our measurement techniques and image processing algorithms allow us to track small disturbance waves traveling along the Taylor bubble interface. The specific mechanisms generating these waves are not relevant for the present study. However, assuming that most of the waves are produced by random disturbances, they are expected to travel in all directions parallel to the air-water interface. The velocities of these waves are governed by the capillary wave equations, as described in [4]. The dispersion relation of capillary waves can be expressed as:

$$\omega^2 = \frac{\sigma k^3}{\rho} \tanh(k\, d)\,,$$

where $k = 2\pi/\lambda$ is the wave number, $\omega = 2\pi\nu$ angular frequency, and $c = \lambda\nu$ is the phase velocity. For typical "thick" 2 mm liquid film waves, the characteristic frequencies, wavelengths, and phase velocities are approximately 1 Hz, 50 mm, and 0.05 m/s, respectively. For the thinner 0.5 mm liquid film, these values are approximately 40 Hz, 5 mm, and 0.2 m/s. These estimates indicate that the characteristic phase velocities of the waves are lower than the interface velocity, implying that practically all waves on the interface travel downward.

To estimate the axial velocities of the disturbance waves traveling over the interface, measurements of the axial disturbance wave velocity $w$ are performed using cross-correlations of the time signals at various axial positions along the pipe. By selecting a distance $H$ between specific points in space, for example, $H$ = 200 pixels, the velocity $w$ can be obtained from the measured time lag $\tau$ of the signals as $w = H/\tau$. For example, the time lag at the point 400 pixels downstream of the bubble nose and at a distance $H$ = 200 pixels, is computed from the cross-correlation of time signals at points 400 - $H/2$ = 300 pixels and 400 + $H/2$ = 500 pixels.

The top diagram in Figure 6 presents the approximated time and left-right averaged velocity of the liquid-air interface, denoted as $v_i(z)(z)$, which is obtained from the measured liquid film thickness $h(z)$ and the continuity equation. The approximation

formula is $v_i(z) = 1.15 \, v_0 R^2 / [2Rh(z) - h(z)^2]$ , where $v_0$ is the mean liquid velocity upstream, and $R$ is the pipe radius. The factor of 1.15 is based on our DNS (Direct Numerical Simulation) results obtained in an infinite turbulent flume flow at similar Reynolds numbers [16]. It applies to the free liquid surface near an infinite flat wall and disregards the air shear force. Each curve obtained from the continuity equation is accompanied by a single uncertainty bar, which reflects the absolute uncertainty in film thickness measurement and recognition, approximately 1 pixel, dominating over other sources of uncertainty.

The bottom image in Figure 6 illustrates velocity profiles of the disturbance waves along the five Taylor bubbles listed in Table 1. These profiles are derived from the time lags observed in the right-hand side of the silhouettes. The complete time histories consisting of 50,000 frames are analyzed for all cases, corresponding to 1, 2, and 4 minutes for measurements at 800, 400, and 200 Hz, respectively. Cross-correlations are compared at a fixed distance of $H = 80$ pixels, and the discrete values of cross-correlation time lags are smoothed using parabolic interpolation.

Both graphs in Figure 6 present two distinct types of velocity profiles obtained from the same measurements but through entirely different analyses. The curves in the top image are directly derived from the absolute measurement of the liquid film thickness combined with the continuity equation, incorporating the empirical correction coefficient of 1.15. On the other hand, the disturbance wave velocities displayed in the bottom image are determined based on the relative motions of the liquid-air interface. Notably, both types of velocities exhibit remarkable similarity. This observation leads us to propose a hypothesis that the time-averaged velocity of the disturbance waves on the water-air interface effectively represents the velocity of the interface itself.

The equivalence between the time-averaged velocities of the interface waves and the convective velocity of the interface, while seemingly excluding the contribution of capillary waves that are expected to travel in all directions, can be explained through several factors. Firstly, the time signals obtained from sufficiently long measurements encompass capillary waves of all frequencies that can propagate in various axial and azimuthal directions. However, the process of time averaging employed in our cross-correlation analysis effectively cancels out the random directions of the disturbance waves.

Furthermore, the characteristic velocities of the dominant waves are significantly lower, at least by an order of magnitude, compared to the mean velocities of the liquid film (approximately 1 m/s). As a result, the time averaging process predicts the final disturbance wave velocity equal to the time-averaged convective velocity of the water-air interface.
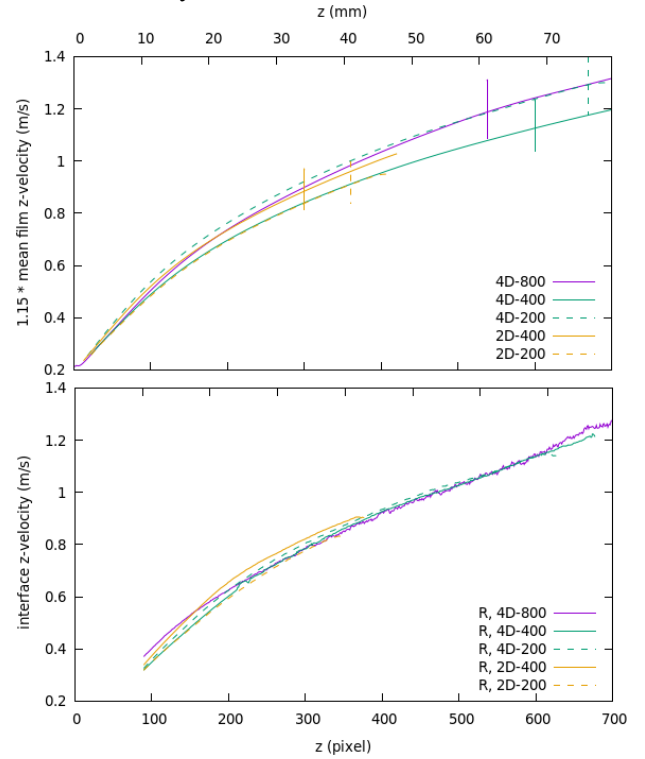


*Fig. 6: Top: liquid film interface velocity profiles from film thickness measurements and continuity equation normalized to liquid mean velocity upstream of the bubble 0.18 m/s. Bottom: Interface velocities from disturbance wave propagation. H = 80 pixels.*

It is important to note that the random nature of the disturbance waves is not obvious. While we acknowledge the potential of the disturbance wave velocity measurement method as a means of directly determining the velocity of the liquid-gas interface, we also intend to validate our hypothesis through additional experiments and accurate numerical simulations.

## IV. Conclusions

In this paper, our focus is on studying the interface of the Taylor bubble in a vertical turbulent counter-current air-water flow, excluding the bubble's tail region. To analyze the bubble interface, we developed in-house computer codes that convert digital

photographs of Taylor bubbles into two-dimensional silhouettes with an absolute uncertainty around 1 pixel and roughly five times lower relative uncertainty.

Our primary goal was to obtain the time-averaged shape of the Taylor bubble interface. However, we discovered that relying solely on time averaging of two-dimensional silhouettes was not sufficient due to the "quasi-stable" nature of the bubble in counter-current flow. The eccentric position of the bubble's nose, which was randomly established during the bubble injection transient, remained unchanged for several minutes in a specific experimental case. The initial azimuthal positions of the Taylor bubbles were found to be stochastic. To obtain the averaged bubble shape, including azimuthal direction averaging, we used ensemble averaging of multiple time-averaged cases. Nonetheless, uncertainties remained significant, potentially limiting comparisons with similar experiments or accurate simulations. We believe that obtaining the final shape of the time-averaged bubble, while retaining axial asymmetry, would require three-dimensional imaging.

The second part of our study is based on the high relative accuracy of our interface reconstruction technique, which was almost an order of magnitude more accurate than the absolute accuracy. This enabled us to develop a method based on cross-correlation of film thickness temporal development measured at different axial locations of the bubble. This method predicts the velocities of disturbance waves traveling over the Taylor bubble's body. Our analyses consistently indicate that the disturbance wave velocity, measured over a sufficiently long interval of several dozen seconds, becomes equal to the axial water-air interface velocity. The cross-correlation measurements primarily capture low-frequency waves, which are slower than the interface velocity. Therefore, tracking these waves provides a technique for measuring the time-averaged interface velocity.

We plan to validate the results of this paper in the near future by conducting high-fidelity LES+VOF simulations of the Taylor bubble. Additionally, we anticipate further testing of our hypothesis on the equality of the interface velocity and interface disturbance waves by combining captured videos with PIV analyses of liquid velocity fields.

## Acknowledgments

## References

1. Wallis G.B. One-Dimensional Two-Phase Flow, McGraw Hill, 1969.
2. Morgado, A.O., Miranda, J.M., Araújo, J.D.P., Campos, J.B.L.M., 2016. Review on vertical gas-liquid slug flow. Int. Journal of Multiphase Flow 85, 348-368.
3. Zhou, G., Prosperetti, A., 2019. Violent expansion of a rising Taylor bubble. Phys. Rev. Fluids 4, 073903.
4. Liberzon, D, Shemer, L, Barnea, D. 2006. Upward-propagating capillary waves on the surface of short Taylor bubbles. Physics of Fluids 18, 048103.
5. Dumitrescu, D.T., 1943. Strömung an einer Luftblase im senkrechten Rohr. Z. angew. Math. Mech. 23, 139.
6. Martin, C.S., 1976. Vertically Downward Two-Phase Slug Flow. ASME J. Fluids Eng., Dec 1976, 98(4): 715.
7. Lu, X., Prosperetti, A. 2006. Axial stability of Taylor bubbles. J. Fluid Mech. 568, 173-192.
8. Delfos, R, Wisse, C.J., Oliemans, R.V.A., 2001. Measurement of air-entrainment from a stationary Taylor bubble in a vertical tube. International Journal of Multiphase Flow 27, 1769-1787.
9. Kockx, J.P., Nieuwstadt, F.T.M., Oliemans, R.V.A., Delfos, R., 2005. Gas entrainment by a liquid film falling around a stationary Taylor bubble in a vertical tube. Int. Journal of Multiphase Flow 31, 1-24.
10. Mikuž B., Kamnikar, J., Prošek, J., Tiselj, I., 2019. Experimental Observation of Taylor Bubble Disintegration in Turbulent Flow. Proc. 28th Int. Conf. Nuclear Energy for New Europe 9.
11. Pan, L., He, H., Ju, P., Hibiki, T., Ishii, M., 2015. Experimental study and modeling of disturbance wave height of vertical annular flow. International Journal of Heat and Mass Transfer 89, 165-175.
12. Lin, R., Wang, K., Liu, L., Zhang, Y., Dong, S, 2020. Study on the characteristics of interfacial waves in annular flow by image analysis. Chemical Engineering Science 212, 115336.
13. Frederix, E.M.A., Komen, E.M.J., Tiselj, I., Mikuž, B., 2020. LES of Turbulent Co-current Taylor Bubble Flow. Flow Turbulence Combust 105, 471-495.
14. Press W.H., Teukolsky, S.A., Vetterling, W.T., Flannery B.P. 2007. Numerical Recipes 3rd Edition: The Art of Scientific Computing, Cambridge Press, 2007.
15. Grishchenko, D., 2011. KROTOS image analysis for water-corium interactions (KIWI), OECD SERENA project report DEN/DTN/STRI/LMA/NT/2011/009/0, CEA, France.
16. Bergant, R, Tiselj, I, 2007. Near-wall passive scalar transport at high Prandtl numbers, Physics of Fluids 19, 065105.
17. Kren, J., Zajec, B., Tiselj, I., El Shawish, S., Perne, Ž., Tekavčič, M., Mikuž, B. 2023. Dynamics of Taylor bubble interface in vertical turbulent counter-current flow. Int. J. Multiphase Flow 165, 104482.